Chapter 6

Quantum Transport in Graphene Quantum Dots

Hai-Ou Li, Tao Tu, Gang Cao, Lin-Jun Wang,
Guang-Can Guo and Guo-Ping Guo

Additional information is available at the end of the chapter

http://dx.doi.org/10.5772/52873

1. Introduction

Graphene exhibits unique electrical properties and offers substantial potential as building blocks of nanodevices owing to its unique two-dimensional structure (Geim et al., 2007; Geim et al., 2009; Ihn et al., 2010). Besides being a promising candidate for high performance electronic devices, graphene may also be used in the field of quantum computation, which involves exploration of the extra degrees of freedom provided by electron spin, in addition to those due to electron charge. During the past few years, significant progress has been achieved in implementation of electron spin qubits in semiconductor quantum dots (Hanson et al., 2007; Hanson et al., 2008). To realize quantum computation, the effects of interactions between qubits and their environment must be minimized (Fischer et al., 2009). Because of the weak spin-orbit coupling and largely eliminated hyperfine interaction in graphene, it is highly desirable to coherently control the spin degree of freedom in graphene nanostructures for quantum computation (Trauzettel et al., 2007; Guo et al., 2009). However, the low energy quasiparticles in single layer grapheme behave as massless Dirac fermions (Geim et al., 2007; Geim et al., 2009), and the relativistic Klein tunneling effect leads to the fact that it is hard to confine electrons within a small region to form quantum dot in graphene using traditional electrostatical gates (Ihn et al., 2010; Trauzettel et al., 2007). It is now possible to etch a grapheme flake into nano-constrictions in size, which can obtain electron bound states and thus act as quantum dots. As a result, usually a diamond-like characteristic of suppressed conductance consisting of a number of sub-diamonds is clearly seen (Stampfer et al., 2009; Gallagher et al., 2010), indicating that charge transport in the single graphene quantum dot device may be described by the model of multiple graphene quantum dots in series along the nanoribbon. The formation of multiple quantum dot structures in the nanoribbons may be attributed to edge roughness or local potential. The rough edges also lift the valley degeneracy, which could suppress the exchange coupling between spins in the grapheme quantum dots (Trauzettel et al., 2007; Ponomarenko et al., 2008). Recently, there was a

striking advance on experimental production of graphene single (Ponomarenko et al., 2008; Stampfer et al., 2008a; Stampfer et al., 2008 b; Schenz et al., 2009; Wang et al., 2010; Guttinger et al., 2011) or double quantum dots (Molitor et al., 2009; Molitor et al., 2010; Liu et al., 2010; Wang et al., 2011a; Volk et al., 2011; Wang et al., 2012;) which is an important first step towards such promise.

In this chapter, we introduce the design and fabrication of etched gate tunable single and double quantum dots in single-layer and bilayer graphene and present several important quantum transport measurements in these systems. A quantum dot with an integrated charge sensor is becoming a common architecture for a spin or charge based solid state qubit. To implement such a structure in graphene, we have fabricated a twin-dot structure in which the larger QD serves as a single electron transistor (SET) to read out the charge state of the nearby gate controlled small QD. A high SET sensitivity allowed us to probe Coulomb charging as well as excited state spectra of the QD, even in the regime where the current through the QD is too small to be measured by conventional transport means (Wang et al., 2010; Wang et al., 2011b). We also have measured quantum transport properties of gates controlled parallel-coupled double quantum dots (PDQD) and series-coupled double quantum dots (SDQD) device on both single layer and bilayer graphene (Wang et al., 2011a; Wang et al., 2012). The inter-dot coupling strength can be effectively tuned from weak to strong by in-plane plunger gates. All the relevant energy scales and parameters can be extracted from the honeycomb charge stability diagrams. We precisely extract a large inter-dot tunnel coupling strength for the series-coupled quantum dots (SDQD) allowing for the observation of tunnel-coupled molecular states extending over the whole double dot. The present method of designing and fabricating graphene QD is demonstrated to be general and reliable and will enhance the realization of graphene nanodevice and desirable study of rich QD physical phenomena in grapheme. These results demonstrate that both single and double quantum dots in single-layer and bilayer graphene bode well for future quantum transport study and quantum computing applications. The clean, highly controllable systems serves as an essential building block for quantum devices in a nuclear-spin-free world.

2. A graphene quantum dot with a single electron transistor as an integrated charge sensor

The measurement of individual electrons or its spins in GaAs quantum dots (QDs) has been realized by so-called charge detection via a nearby quantum point contact (QPC) or single electron transistor (SET) (Lu et al., 2003; Elzerman et al., 2004a). In particular, the combination of high speed and high charge sensitivity has made SET useful in studying a wide range of physical phenomena such as discrete electron transport (Lu et al., 2003; Bylander et al., 2005; Gotz et al., 2008), qubit read out (Lehnert et al., 2003; Duty et al., 2004; Vijay et al., 2009) and nanomechanical oscillators (Knobel et al., 2003; Lahaye et al., 2004). So far, most SETs have been using Al/AlO_x/Altunnel junctions. However, the graphene SET reported here is technologically simple and reliable, making it an attractive substitute for use in various charge detector applications.

In this section, we realize an all graphene nanocircuit integration with a SET as charge read out for a QD. In conventional semiconductor systems, the gate-defined structure limits the distance be-

http://dx.doi.org/10.5772/52873

tween the QD and the detector. However, in our device reported here, the QD and the SET in the same material are defined in a single etching step, and the distance between the graphene nanostructures is determined by the etched area, which enables optimized coupling and sensing ability. The SET is placed in close proximity to the QD giving rise to a strong capacitive coupling between the two systems. Once an additional electron occupies the QD, the potential in the neighboring SET is modified by capacitive interaction that gives rise to a measurable conductance change. Even if charge transport through the QD is too small to be measured by conventional transport means, the SET charge sensor also allows measurements. These devices demonstrated here provide robust building blocks in a practical quantum information processor.

The graphene flakes were produced by mechanical cleaving of graphite crystallites by Scotch tape and then were transferred to a highly doped Si substrate with a 100 nm SiO_2 top layer. Thin flakes were found by optical microscopy, and single layer graphene flakes were selected by the Raman spectroscopy measurement. We used the standard electron beam lithography and lift off technique to make the Ohmic contact (Ti/Au) on the present graphene devices. Next, a new layer of polymethyl methacrylate is exposed by electron beam to form a designed pattern. Then, the unprotected areas are removed by oxygen reactive ion etching. One of our defined sample structures with a quantum dot and proximity SET is shown in Fig. 1. The quantum dot is an isolated central island of diameter 90 nm, connected by 30nm wide tunneling barriers to source and drain contacts. Here, the Si wafer was used as the back gate and there is also a graphene side gate near the small dot. The SET has a similar pattern while the conducting island has a much larger diameter (180nm). Electronic transport through both the devices exhibits Coulomb blockade (CB) characteristics with back/side gate voltage. The distance between the CB peaks is determined by the sum of charging and quantum confinement energies, and the former contribution becomes dominant for our devices with diameter >100nm (Kouwenhoven et al., 1997). Accordingly, we refer to it as a SET rather than a QD. The device was first immersed into a liquid helium storage Dewar at 4.2K to test the functionality of the gates. The experiment was carried out in a top-loading dilution refrigerator equipped with filtered wiring and low-noise electronics at the base temperature of 10 mK. In the measurement, we employed the standard ac lock-in technique.

Fig. 2(a) shows the conductance through the dot $Al/AlO_x/Al$ for applied side gate voltage V_{sg}. Clear CB peaks are observed related to charging of the tunable dot on the graphene. The dashed green lines in the range of 0.2-0.7V for side gate voltages show that the current through the dot becomes too small to be seen clearly. Fig. 2(b) shows the conductance through the SET versus side gate voltage V_{sg}. The SET is as close as possible to the QD and in this way charging signals of the dot were detected by tracking the change in the SET current. The addition of one electron to the QD leads to a pronounced change of the conductance of the charge detector by typically 30%. The slope of the SET conductance is the steepest at both sides of its CB resonances giving the best charge read-out signal. To offset the large current background, we used a lock-in detection method developed earlier for GaAs dot (Elzerman et al., 2004b). A square shaped pulse was superimposed on the dc bias on side gate voltage V_{sg}. A lock-in detector in sync with the pulse frequency measured the change of SET current due to the pulse modulation. Fig. 2(c) shows a typical trace of the lock-in signal of the transconductance through the SET dI_{SET}/dV_{sg}. These sharp spikes or dips originate from the change of the charge on the dot by one electron. It shows essentially the same features as Fig. 2(a), but is much richer, especially in the regime where the direct dot current is too

small to be seen clearly. The vertical dashed lines in Fig. 2 illustrate the SET sensor signals correspond to the QD transport measurements perfectly and indicate the SET is reliable. We also note that the individual charge events measurement has been demonstrated in a graphene QD with a QPC detector based on graphene nanoribbon (Güttinger et al., 2008).

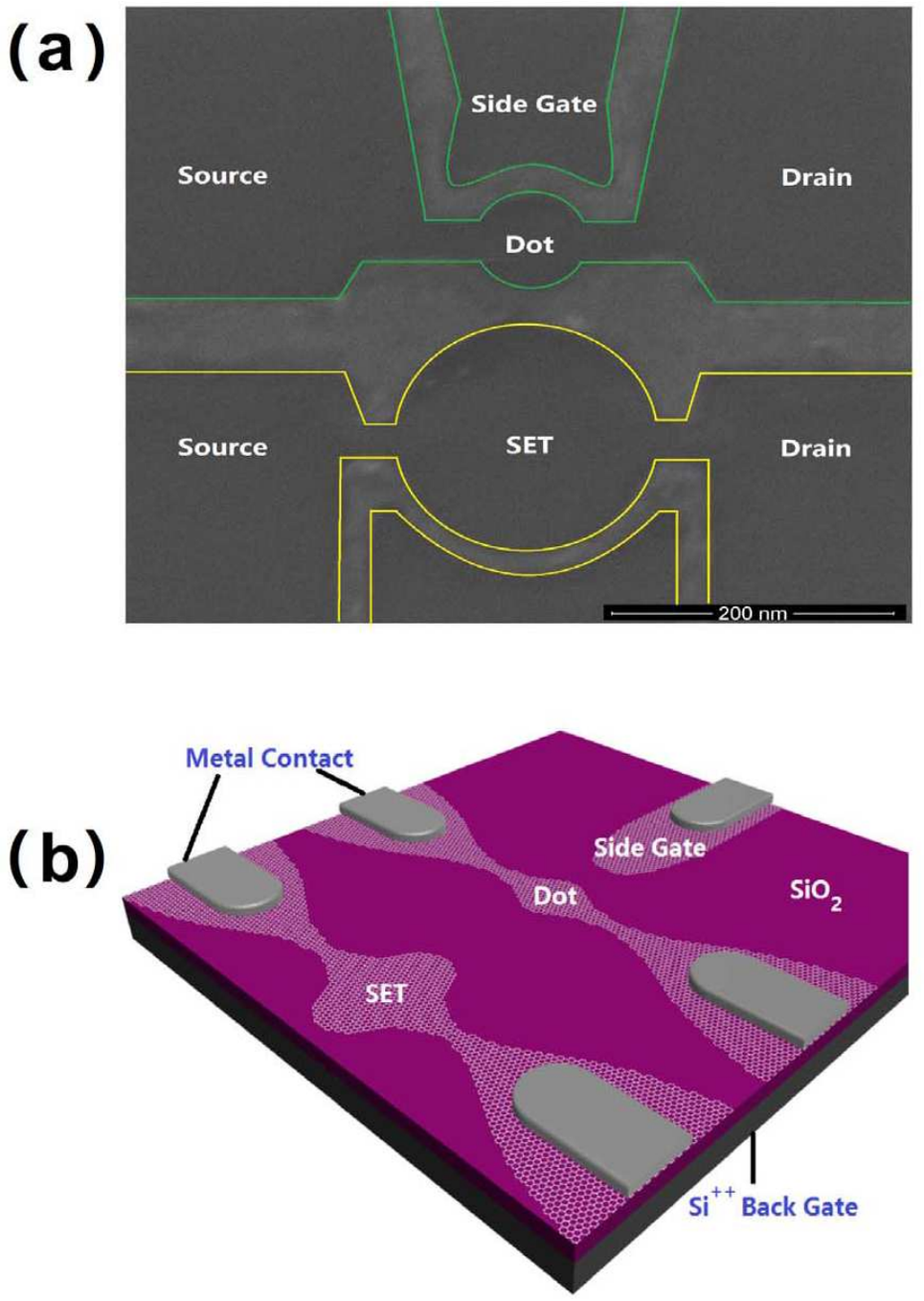

Figure 1. a) Scanning electron microscope image of the etched sample structure. The bar has a length of 200 nm. The upper small quantum dot as the main device has a diameter of 90 nm while the bottom single electron transistor as charge sensor has a diameter of 180 nm. The bright lines define barriers and the graphene side gate. (b) Schematic of a representative device.

http://dx.doi.org/10.5772/52873

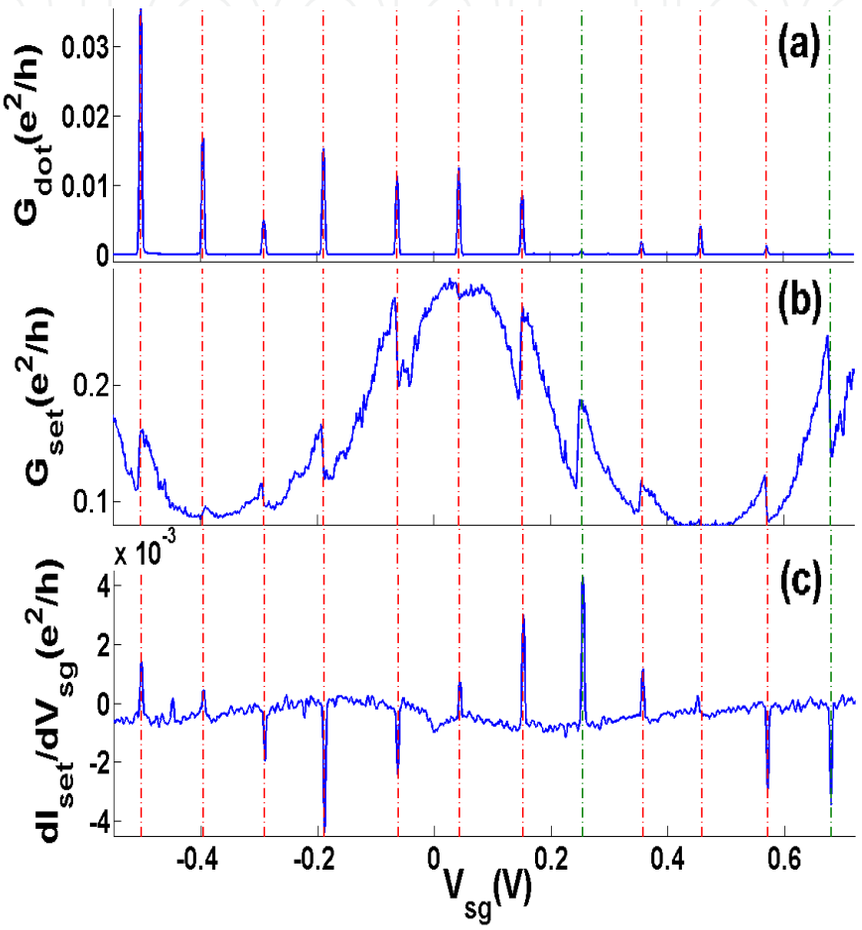

Figure 2. a) Conductance through the quantum dot vs the side gate voltage. (b) The example of conductance through the single electron transistor for the same parameter ranges as in panel (a). The steps in conductance have about 30% change of the total signal and are well aligned with the CB in panel (a). (c) Transconductance of the single electron transistor for the same parameters as in panel (a). The spikes and dips indicate the transitions in the charge states by addition of single electron in quantum dot. In particular, the dashed green lines show that the charge detection can allow measurement in the regime where the current through the dot is too small to be seen clearly by direct means. The vertical dashed red lines are a guide for the eyes to relate features in these graphs.

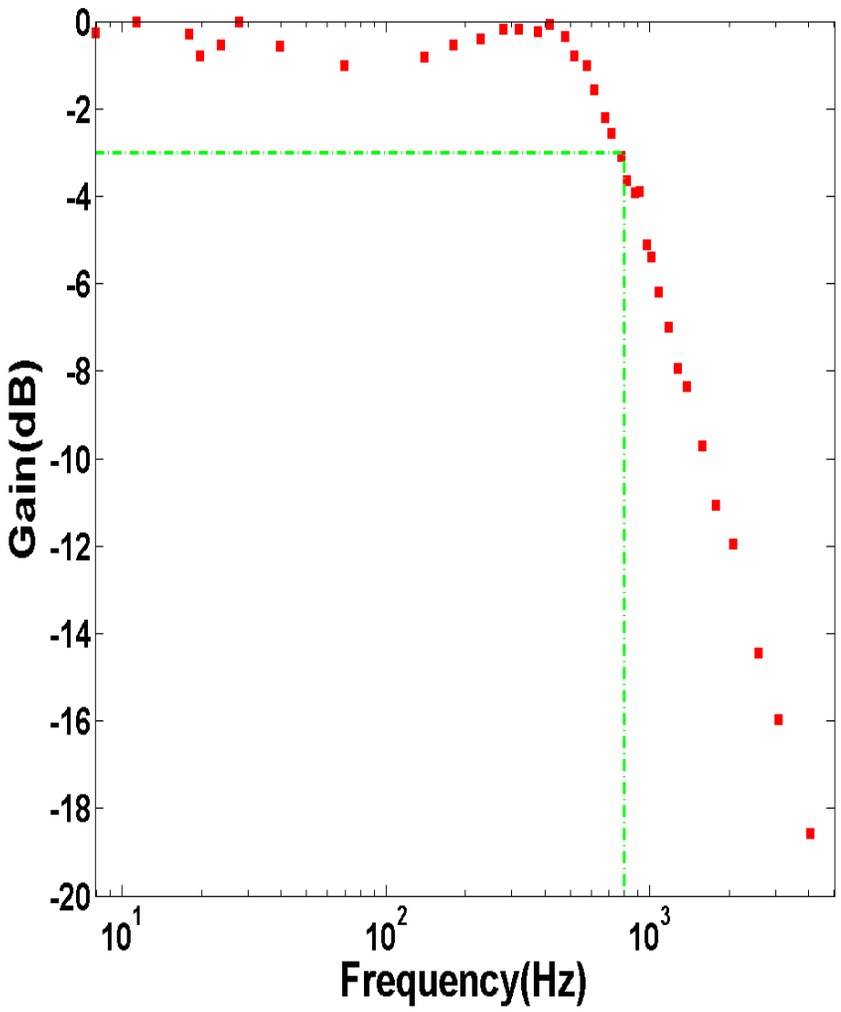

Figure 3. The magnitude of the SET signal dI_{SET}/dV_{sg} as a function of the modulating pulse frequency. The dashed green line illustrates that the bandwidth of the SET device is about 800 Hz corresponding to a gain of 0.707(-3 dB). Due to the stray capacitances, the response decreases rapidly after 800 Hz.

http://dx.doi.org/10.5772/52873

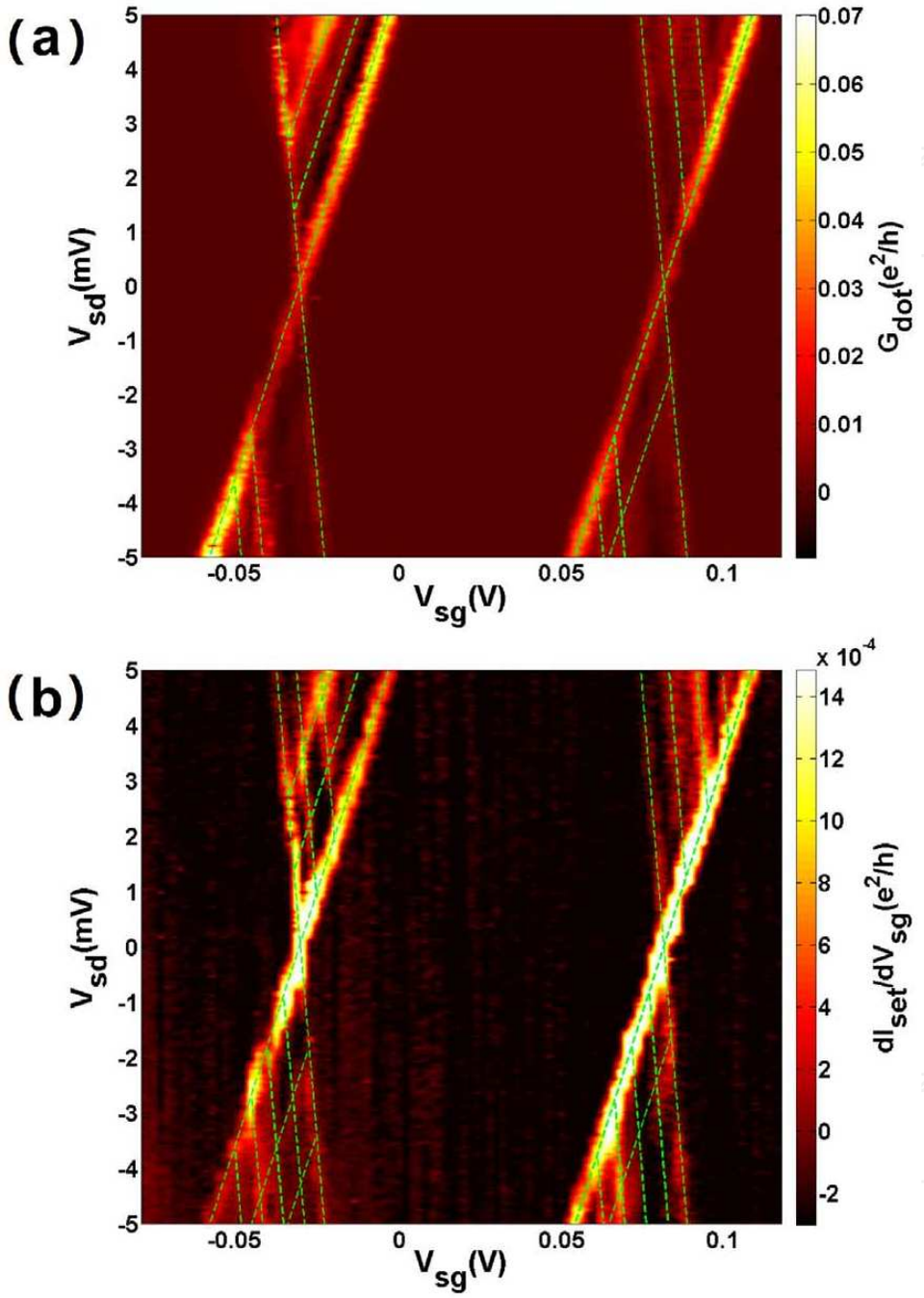

Figure 4. a) Plot of the differential conductance of the quantum dot as a function of the bias voltage and the side gate voltage applied on the dot. From the lines parallel to the edges of Coulomb diamonds, we can identify the excited states. (b) Transconductance of the single electron transistor with the same parameters as in panel (a). Perfect matching with panel (a) and resolving more excited states spectra indicate that the single electron transistor can be used as a highly sensitive charge detector. Data in panels (a) and (b) were recorded simultaneously during a single sweep. Dashed green lines are the guide for identifying the excited states.

More quantitative information on the system can be obtained from the measurement of the height response of the peak at 0.152 V in Fig. 2(c) as a function of the modulating pulse frequency on the side gate. The resulting diagram for the SET dI_{SET}/dV_{sg} gain magnitude is shown in Figure 3.The dashed green line indicates the gain of 0.707 (-3 dB), corresponding approximately to the bandwidth of 800 Hz of the SET device. By applying a signal of 5×10^{-2} electrons on back gate of the SET and measuring the signal with a signal-to-noise ratio of 1, we achieved a charge sensitivity $10^{-3}e/\sqrt{Hz}$ of which is similar to that obtained previously in a GaAs QD and superconducting Al SET detector system (Berman et al., 1999). The system can be simply considered as a resistor-capacitor circuit (RC circuit), and the bandwidth is limited by the resistor and capacitance of the cable connecting the SET and the room temperature equipments. As a result, we would expect the bandwidth can be greatly improved by adding a cold amplifier (Vink et al., 2007). It is also expected that adding a side gate near the SET to independently set the SET operating point to about 25 kΩ can obviously enhance the bandwidth.

The information contained in the signal goes beyond simple charge counting. For instance, the stability diagram measurement can reveal excited states, which is crucial to get information of the spin state of electrons on a quantum dot (Hanson et al., 2003). Fig. 4(a) shows Coulomb diamonds for the conductance through the dot GQD versus bias voltage V_{sd} and side gate voltage V_{sg}. For comparison, Fig. 4(b) shows the transconductance of the SET dI_{SET}/dV_{sg} as a function of the same parameters. A perfect match between the QD transport measurements and the detector signal is observed. Moreover, the discrete energy spectra of the graphene quantum dot are revealed by the presence of additional lines parallel to the diamond edges. These lines indicate the quantum dot is in the high bias regime where the source-drain bias is high enough that the excited states can participate in electron tunneling (Hanson et al., 2007). The excited states become much more visible in the SET charge detector signal than the direct measurement. All of these features have been seen in GaAs QD with QPC (Hanson et al., 2007), but here we achieve the goal with an all graphene nanocircuit of QD with SET. In the previous reports, the QD and QPC detector are separated by typically 100 nm in width. In the present case, the SET detector is 50 nm from the edge of the QD. Therefore it is expected that the capacitance coupling between QD and SET is enhanced compared to the conventional case realized in semiconductor QD and QPC. This enhanced coupling leads to a larger signal-to-noise ratio of the SET detector signal that can be exploited for time resolved charge measurement or charge/spin qubit read out on the QD.

In summary, we have presented a simple fabrication process that produces a quantum dot and highly sensitive single electron transistor charge detector with the same material, graphene. Typically the addition of a single electron in QD would result in a change in the SET conductance of about 30%. The charging events measured by both the charge detector and direct transport through the dot perfectly match and more excited states information beyond the conventional transport means is also obtained. The devices demonstrated here represent a fascinating avenue towards realizing a more complex and highly controllable electronic nanostructure formed from molecular conductors such as graphene.

http://dx.doi.org/10.5772/52873

3. Controllable tunnel coupling and molecular states in a graphene double quantum dot

Previously, the charge stability diagram in coupled quantum-dot systems has been studied by the classical capacitance model (van der Wiel et al., 2003). However the quantum effect should also manifest itself (Yang et al., 2011). In particular, the tunnel coupling *t* between the two dots in a double dot is an important quantity, because it can affect the geometry of the overall charge stability diagram. Furthermore, several different spin qubit operations can be performed by controlling this tunnel rate as a function of time. For approaches based on single electron spin qubit, utilizing t enables the $\sqrt{\text{SWAP}}$ gate operations between two qubits (Petta et al., 2005). In an architecture in which each qubit is composed of two-electron single-triplet states, control of t in the presence of a non-uniform magnetic field enables universal single qubit rotations (Foletti et al., 2009).

In this Section, we report an experimental demonstration and electrical transport measurement in a tunable graphene double quantum dot device. Depending on the strength of the inter-dot coupling, the device can form atomic like states on the individual dots (weak tunnel coupling) or molecular like states of the two dots (strong tunnel coupling). We also extract the inter-dot tunnel coupling t by identifying and characterizing the molecule states with wave functions extending over the whole graphene double dot. The result implies that this artificial grapheme device may be useful for implementing two-electron spin manipulation.

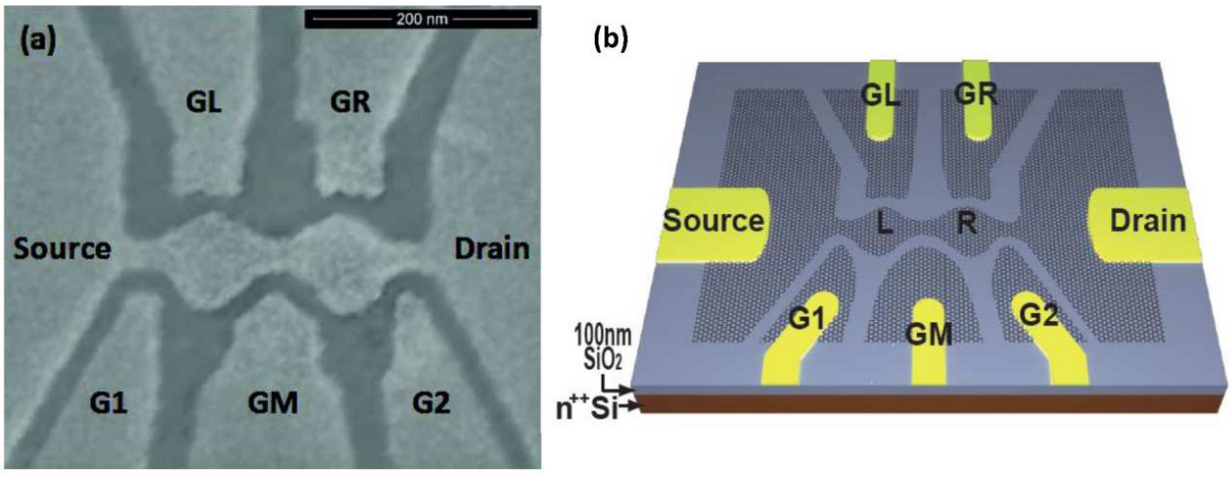

Figure 5. a) Scanning electron microscope image of the structure of the designed multiple gated sample studied in this work. The double quantum dot have two isolated central islands of diameter 100 nm in series, connected by 20×20 nm tunneling barriers to source and drain contacts (S and D) and 30×20 nm tunneling barrier with each other. These gates are labeled by G1, GL, GM, GR, G2, in which gate GM, G1 and G2, are used to control the coupling barriers between the dots as well as the leads. Gates GL and GR are used to control and adjust the energy level of each dot. (b) Schematic of a representative device.

A scanning electron microscope image of our defined sample structure with double quantum dot is shown in Fig. 5(a) and Fig. 5(b). The double quantum dot has two isolated central

island of diameter 100 nm in series, connected by 20× 20 nm narrow constriction to source and drain contacts (S and D electrodes) and 30× 20 nm narrow constriction with each other. These constrictions are expected to act as tunnel barriers due to the quantum size effect. In addition, the highly P-doped Si substrate is used as a back gate and five lateral side gates, labeled the left gate G1, right gate G2, center gate GM and GL(R), which are expected for local control. All of side gates are effective, in which gates GL, GR and G2 have very good effect on two dots and middle barrier, while gates G1 and GM have weak effect on those. The device was first immersed into a liquid helium storage dewar at 4.2K to test the functionality of the gates. The experiment was carried out in a He3 cryostat equipped with filtered wiring and low-noise electronics at the base temperature of 300mK. In the measurement, we employed the standard AC lock-in technique with an excitation voltage 20 μVat 11.3 Hz.

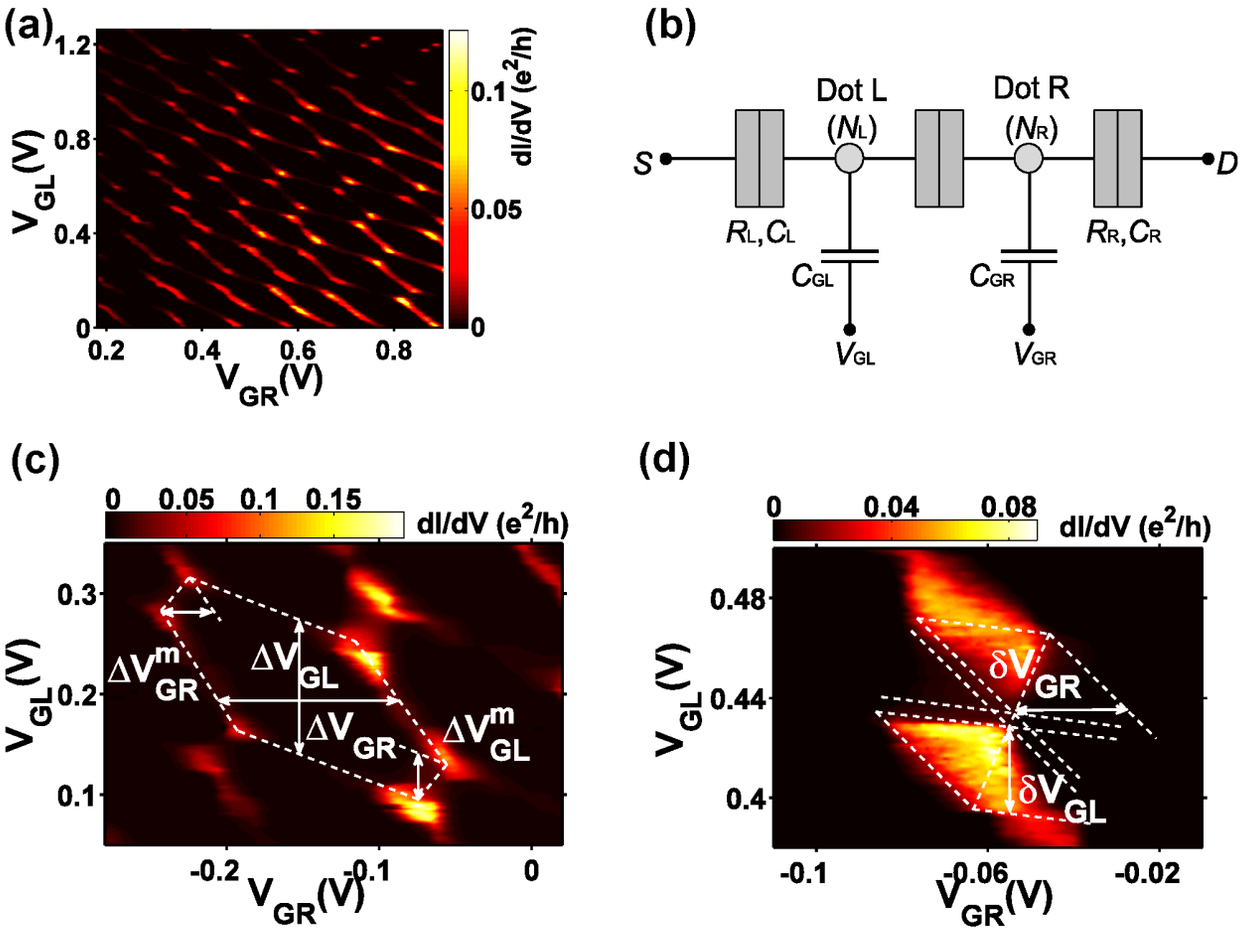

Figure 6. a) Color scale plot of the differential conductance versus voltage applied on gate GL (V_{GL}) and gate GR (V_{GR}) at V_{sd}= 20μV, V_{G1} = 0V, V_{GM} = 0V, V_{G2} = 0V and V_{bg} = 2.5 V. The honeycomb pattern we got stands for the typical charge stability diagram of coupled double quantum dots. (b) Pure capacitance model of a graphene double dot system. Zoom in of a honeycomb structure (c) and a vertex pair (d) at V_{sd} = 900μV.

Fig. 6(a) displays the differential conductance through the graphene double quantum dot circuit as a function of gate voltages V_{GL} and V_{GR}. Here the measurement was recorded at

V_{sd}= 20μV, V_{G1} = 0V, V_{GM} = 0V, V_{G2} = 0V and V_{bg} = 2.5 V. The honeycomb pattern is clearly visible and uniforms over many times. Each cell of the honeycomb corresponds to a well-defined charge configuration (NL,NR) in the nearly independent dots, where NL and NR denote the number of electrons on the left and right dot, respectively. The conductance is large at the vertices, where the electrochemical potentials in both dots are aligned with each other and the Fermi energy in the leads and resonant sequential tunneling is available. These vertices are connected by faint lines of much smaller conductance along the edges of the honeycomb cells. At these lines, the energy level in one dot is aligned with the electrochemical potential in the corresponding lead and inelastic cotunneling processes occur. The observed honeycomb pattern resembles the charge stability diagram found for weakly coupled GaAs double quantum dot (van der Wiel et al., 2003). Such similarities indicate that graphene quantum dot devices will continue to share features with well-studied semiconductor quantum dot systems. The energy-level statistics of single graphene quantum dot was probed and shown to agree well with the theory of chaotic Dirac billiards (Ponomarenko et al., 2008). It is interesting and important to know whether these Dirac fermions' behaviors can be realized and observed in grapheme double quantum dot. Nevertheless, it will be studied in the future work.

More quantitative information such as double dot capacitances can be extracted using a electrostatic model as shown in Fig. 6(b) (van der Wiel et al., 2003). First, the capacitance of the dot to the side gate can be determined from measuring the size of the honeycomb in Fig. 6(c) as $C_{GL} = e/\Delta V_{GL} \approx$1.27aF and$C_{GR} = e/\Delta V_{GR} \approx$1.49aF. Next, the capacitance ratios can be determined from measuring the size of the vertices in Fig. 6(d) at finite bias V_{sd}=900μV as $\alpha_L = |V_{sd}|/\delta V_{GL}$ =0.029 and$\alpha_R = |V_{sd}|/\delta V_{GR}$=0.035. Using the relation $C_{GL}/C_L = \alpha_L$ and $C_{GR}/C_R = \alpha_R$, we can obtain the typical values of dot capacitances as C_L =44.8aFand C_R=44.1aF, respectively. The amount of interdot coupling can be achieved by measuring the vertices splitting in Fig. 6(c). Assuming the capacitively coupling is dominant in the weakly coupled dots regime (van der Wiel et al., 2003; Mason et al., 2004), the mutual capacitance between dots is calculated as

$$C_M = \Delta V_{GL}^m C_{GL} C_R / e = \Delta V_{GR}^m C_{GR} C_L / e = 9.2\text{aF}$$

It has been expected that opening the interdot constriction by gate voltage will cause the tunnel coupling to increase exponentially faster than the capacitive coupling (Kouwenhoven et al., 1997). Fig. 7(a)-(c) represent a selection of such measurements by holding the same V_{GR} and V_{bg} and scanning different ranges of V_{GL} between -0.5 V to 0.35 V. An evolution of conductance pattern indicates that the stability diagram changes from weak to strong tunneling regimes (van der Wiel et al., 2003; Mason et al., 2004). The conductance near the vertices depends on the relative contributions of the capacitive coupling and tunnel coupling. For the former, the vertices become a sharpened point, while for the latter, the vertices become blurred along the edges of the honeycomb cell (Graber et al., 2007). In Fig. 7(b), the vertices is not obvious as those in Fig. 7(a), which indicates a stronger tunnel coupling. The results suggest that two graphene dots are interacting with each other through the large quantum mechanical tunnel coupling, which is analogous to covalent bonding. We will analyze it in details

below. An increase in inter-dot coupling also leads to much larger separation of vertices in Fig. 7(b) (Mason et al., 2004), and finally, to a smearing of honeycomb features in Fig. 7(c). In this case, the double dots behave like a single dot, as illustrated in Fig. 7(g). We note that a similar evolution is observed for four different values of V_{bg} from 2.5 V to 2.0 V at the same V_{GL} and V_{GR} regimes as shown in Fig. 7(d)-(f). Thus the inter-dot tunnel coupling could also be changed by V_{GL} or V_{bg}. This can be explained by the fact that the side gates and back gate may influence the central barrier through the existing capacitances between the gates and the central barrier.

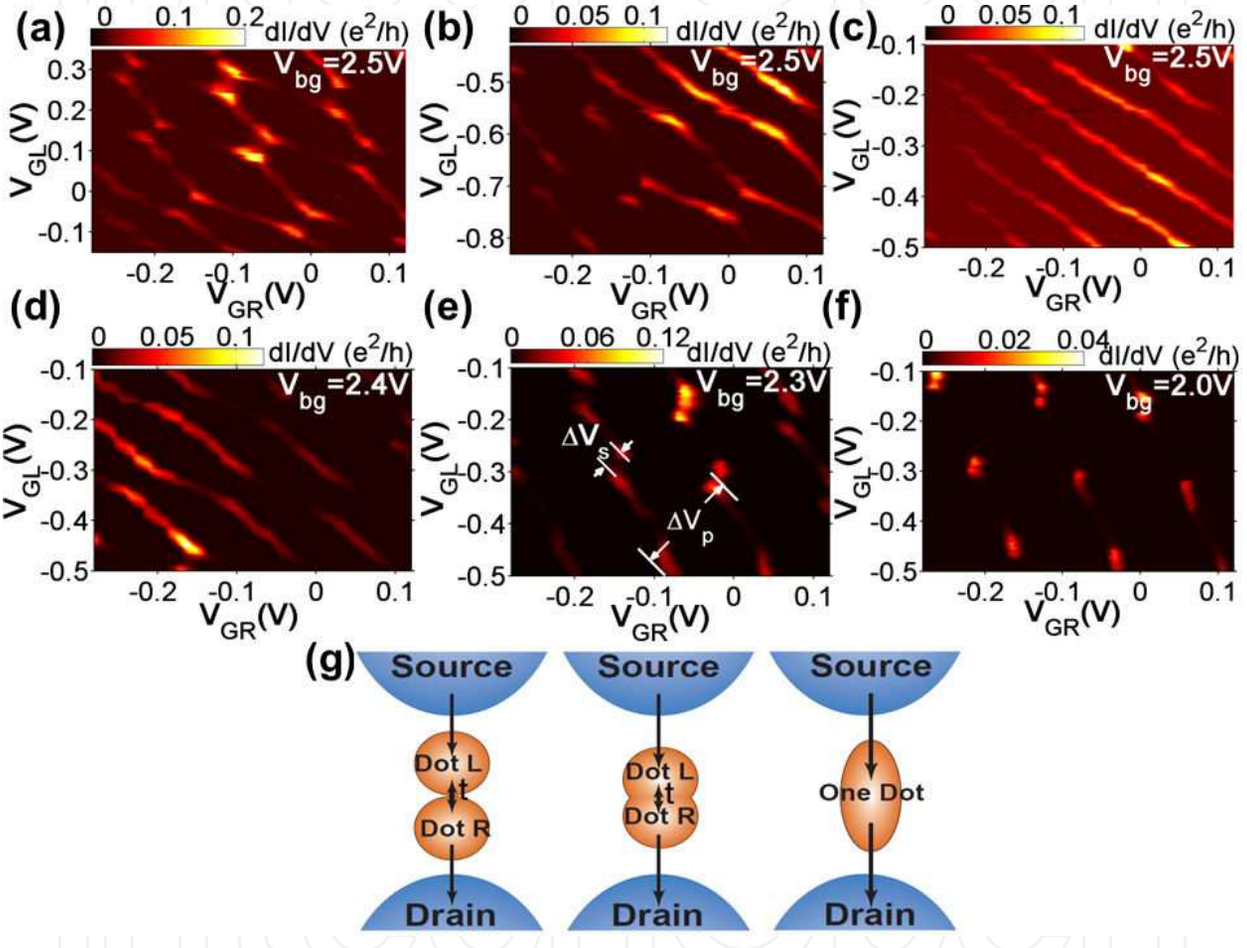

Figure 7. a)-(c) Colorscale plot of the differential conductance versus voltage applied on gate GL (V_{GL}) and gate GR (V_{GR}) at V_{bg} = 2.5 V for different V_{GL} regimes. (d)-(f) Color scale plot of the differential conductance versus voltage applied on gate L (V_{GL}) and gate R(V_{GR}) for different back gate voltage V_{bg}. The trend of interdot tunnel coupling changing from weak to strong can be seen clearly. (g) Sketches of the characteristic electronic configurations with interdot tunnel coupling *t*.

Similar to the definitions in Ref. (Livermore et al., 1996), we define $f = 2\Delta V_S / \Delta V_P$ with ΔV_S representing the splitting between vertices in the diagonal direction and ΔV_P the vertex pairs distance (Fig. 7(e)). Thus, the case $f = 1$ stands for strong coupling limit where the double dots behave like a single dot, while the case $f = 0$ represents weak coupling limit where the double dots behave like two isolated dots. This way, f should have a certain relationship

http://dx.doi.org/10.5772/52873

with tunnel couplings which offers us a method to measure the contribution of the interdot tunneling to the splitting of the vertex. In our double-dot sample, a clear evolution of f is obtained through scanning different regimes of V_{GL} with fixed V_{GR} (Fig. 7(a)-(c)). Through extracting ΔV_S and ΔV_P, we get f =0.5 for (a) and f =0.65 for (b) and f =1 for (c) respectively. These values indicate that control of tunnel coupling as a function of such a gate voltage is conceivable.

Having understood the qualitative behavior of the graphene device in the strong coupling regime, we extract the quantitative properties based on a quantum model of graphene artificial molecule states (Yang et al., 2003; Graber et al., 2007; Hatano et al., 2005). Here we only take into account the topmost occupied state in each dot and treat the other electrons as an inert core (van der Wiel et al., 2003; Golovach et al., 2004). In the case of neglected tunnel coupling, the nonzero conductance can only occur right at the vertices which are energy degenerate points as $E(N_L + 1, N_R) = E(N_L, N_R + 1)$. When an electron can tunnel coherently between the two dots, the eigenstates of the double dot system become the superposed states of two well-separated dot states with the form

$$\left|\psi_B\right\rangle = -\sin\frac{\theta}{2}e^{-\frac{i\varphi}{2}}\left|N_L+1,N_R\right\rangle + \cos\frac{\theta}{2}e^{\frac{i\varphi}{2}}\left|N_L,N_R+1\right\rangle \tag{1}$$

$$\left|\psi_A\right\rangle = \cos\frac{\theta}{2}e^{-\frac{i\varphi}{2}}\left|N_L+1,N_R\right\rangle + \sin\frac{\theta}{2}e^{\frac{i\varphi}{2}}\left|N_L,N_R+1\right\rangle \tag{2}$$

Where $\theta = \arctan(\frac{2t}{\varepsilon})$, $\varepsilon = E_L - E_R$, E_L and E_R are the energies of state $|N_L + 1, N_R\rangle$ and $|N_L, N_R + 1\rangle$, respectively. Thus $|\psi_B\rangle$ and $|\psi_A\rangle$ are the bonding and anti-bonding state in terms of the uncoupled dot, and the energy difference between these two states can be expressed by

$$E_\Delta = \mathrm{U}' + \sqrt{\varepsilon^2 + (2t^2)} \tag{3}$$

Here $\mathrm{U}' = \frac{2e^2 C_m}{C_L C_R - C_m^2}$ is the contribution from electrostatic coupling between dots (Ziegler et al., 2000).

Provided that the graphene double-dot molecule eigenstate $|\psi\rangle$ participates in the transport process, sequential tunneling is also possible along the honeycomb edges. In Fig. 8(a) and Fig. 8(b), a colorscale plot of the differential conductance is shown at $V_{sd} = 20\ \mu$V in the vicinity of a vertex. As expected the visible conductance is observed at both the position of the vertex and the honeycomb edges extending from the vertex. Fig. 8(c) shows a fit of the energy difference E_Δ from the measured mount of splitting of the positions of the differential conductance resonance peak in the ε-direction. Here we use $\varepsilon = E_L - E_R = e\alpha_L V_{GL} - e\alpha_R V_{GR}$ to

translate the gate voltage detuning $V_{GL} - V_{GR}$ with the conversion factors α_L and α_R determined above. The fitting with Eq. (3) yields the values of tunnel coupling strength $t \approx 727\mu$eV and $U' \approx 209\mu$eV. Similar measurements have been performed in a carbon nanotube double dots with $t \approx 358\mu$eV and $U' \approx 16\mu$eV (Graber et al., 2007) and semiconductor double dots with $t \approx 80\mu$eV and $U' \approx 175\mu$eV (Hatano et al., 2005). The fact that the tunnel coupling t is dominant than capacitive coupling U′ implies the inter-dot tunnel barrier in the etched grapheme double dot is much more transparent than those gated carbon nanotube or semiconductor double dot.

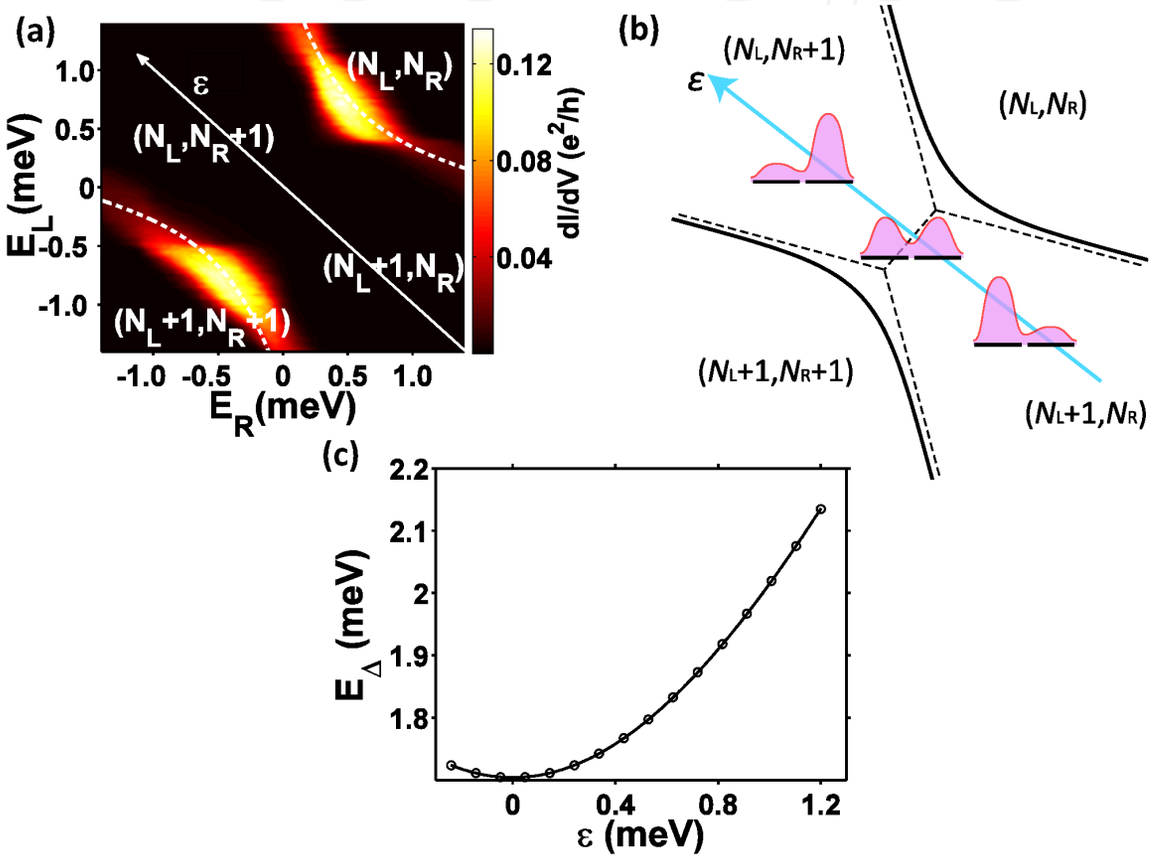

Figure 8. a) Colorscale plot of the differential conductance versus the energies of each dot E_L and E_R at V_{sd} = 20 μV near the selected two vertices with dashed lines as guides to the eye. (b) Schematic of a single anticrossing and the evolution from the state localized in each dot to a molecule state extending across both dots (Hatano et al., 2005). (c) E_Δ dependence of the detuning $\varepsilon = E_L - E_R$ E_Δ (circles) is measured from the separation of the two high conductance wings in Fig. 4(a). The line illustrates a fit of the data to Eq. (3).

Finally, we discuss the relevance of graphene double dot device for implementing a quantum gate and quantum entanglement of coupled electron spins. A $\sqrt{\text{SWAP}}$ operation has already been demonstrated in a semiconductor double dot system using the fast control of exchange coupling J (Petta et al., 2005). The operation time τ is about 180 ps for $J \approx 0.4$meV corresponding to $t \approx 0.16$meV. In the present graphene device, we have obtained much larger $t \approx 0.72$meV and the estimated $\tau \approx 50$ps is much shorter than the predicted decoherence time

http://dx.doi.org/10.5772/52873

(μs) (Fischer et al., 2009). The results indicate the ability to carry out two-electron spin operations in nanosecond timescales on a graphene device, four times faster than perviously shown for semiconductor double dot.

In summary, we have measured a graphene double quantum dot with multiple lectrostatic gates and observed the transport pattern evolution in different gate configurations. This way offers us a method to identify the molecular states as a quantum-mechanical superposition of double dot and measure the contribution of the interdot tunneling to the splitting of the differential conductance vertex. The precisely extracted values of inter-dot tunnel coupling t for this system is much larger than those in previously reported semiconductor device. These short operation times due to large tunneling strength together with the predicted very long coherence times suggest that the requirements for implementing quantum information processing in graphene nanodevice are within reach.

4. Gates controlled parallel-coupled double quantum dot on both single layer and bilayer grapheme

In contrast to DQD in series, where the applied current passes through the double dot in serial, the parallel-coupled double quantum dot (PDQD) requires two sets of entrances and exits, one for each dot. In addition, the source and drain must maintain coherence of the electron waves through both dots, in a manner analogous to a Young's double slit. Thus PDQD is an ideal artificial system for investigating the interaction and interference. Rich physical phenomena, such as Aharonov- Bohm (AB) effect, Kondo regimes and Fano effect, have been predicted to be observed in parallel DQD (Holleitner et al., 2001; Lo´pez et al., 2002; Ladro´n de Guevara et al., 2003; Orellana et al., 2004; Chen et al., 2004). Particularly excitement is the prospect of accessing theoretically predicted quantum critical points in quantum phase transitions (Dias da Silva et al., 2008). The grapheme PDQD is an attractive system for investigating the quantum phase transitions due to its intrinsically large energy separation between on-dot quantum levels, thus offering a significant advantage over conventional systems as GaAs or silicon based quantum dots.

In this section, we present the design, fabrication, and quantum transport measurement of double dot structure coupled in parallel, on both bilayer and single layer grapheme flakes, which may open a door to study the rich PDQD physical phenomena in this material the parallel graphene structure can be tuned from a strong-coupling resulted artificial molecule state to a weak-coupling resulted two-dot state by adjusting in plane plunger gates. The tuning is found to be very reliable and reproducible, with good long-term stability on the order of days.

Graphene flakes are produced by mechanical cleaving of bulk graphite crystallites by Scotch tape (Novoselov et al., 2004). For this kind of exfoliated graphene flakes on SiO_2 substrate, the mobility is normally about 15000 $cm^2/(Vs)$ (Geim et al., 2007). By using heavily doped Si substrate with 100 nm thick SiO_2 on top, we can identify monolayer, bilayer, and few layer graphenes through optical microscope. Monolayer and bilayer gra-

phenes were further checked by Raman spectrum. Firstly, graphene flakes are transferred to the substrate with gold markers. Then, a layer of 50nm thick polymethyl methacrylate (PMMA) is spun on the substrate for electron beam lithography (EBL) to form a designed pattern. After that, O_2/Ar (50:50) plasma is used to remove unprotected parts of graphene. Next, an area of over exposed PMMA is used to separate a bridge plunger gate from the drain part of graphene (Chen et al., 2004; Huard et al., 2007). The final step is to make the metal contacts, which are defined by the standardized EBL process, followed by the E-beam evaporation of Ti/Au (2 nm/50 nm).

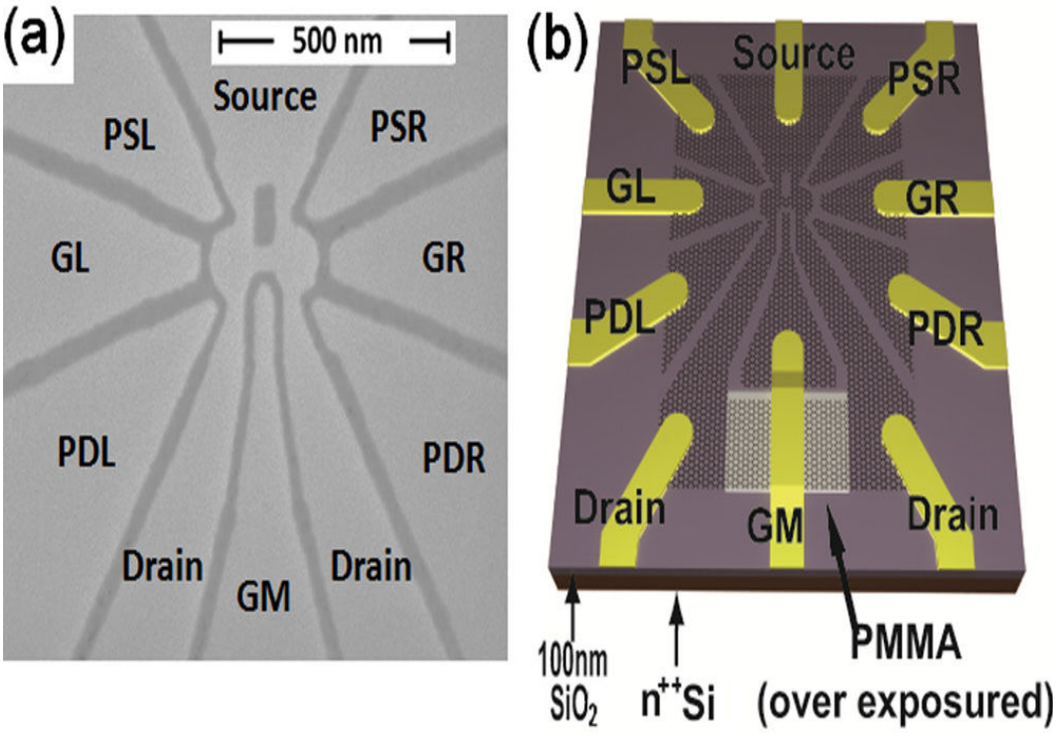

Figure 9. Color online) (a) Scanning electron microscope image of the etched parallel coupled graphene double dot sample structure. The bar has a length of 500 nm. The diameters of the two dots are both 100 nm, constriction between the two dots is 35 nm in width and length. The four narrow parts connecting the dot to source and drain parts have a width of 30 nm. Seven in-plane plunger gates labeled as GL, GR, GM, PSL, PDL, PSR, and PDR are integrated around the dot for fine tuning. (b) Schematic picture of the device. N-type heavily doped silicon substrate is used as a global back gate. A layer of overexposed PMMA is used as a bridge to make gate GM separated from the drain part of graphene.

Fig. 9(a) shows a scanning electron microscope (SEM) image of one sample with the same structure as the bilayer device we measured. Two central islands with diameter of 100 nm connect through 30 nm wide narrow constrictions to the source and the drain regions. Another narrow constriction (35nm in both width and length) connects the two central islands. Seven in-plane plunger gates labeled as GL, GR, GM, PSL, PDL, PSR, and PDR are integrated in close proximity to the dots. GL, GR, and GM are, respectively, designed to adjust the energy level of left dot, right dot, and inter-dot coupling strength. And PSL, PDL (PSR, PDR) are used for the tuning of the coupling of the left (right) dot to source and drain. The

http://dx.doi.org/10.5772/52873

n-type heavily doped silicon substrate is used as a global back gate. The bridge plunger gate GM is separated from the drain part of graphene by a layer of over exposed PMMA. All the devices were primarily tested to check the functionality of all the gates in a liquid helium storage dewar at 4.2 K. Then the samples were mounted on a dilution refrigerator equipped with filtering wirings and low-noise electronics at the base temperature of 10 mK. To maintain consistency, we will use the data from one sample only in the following.

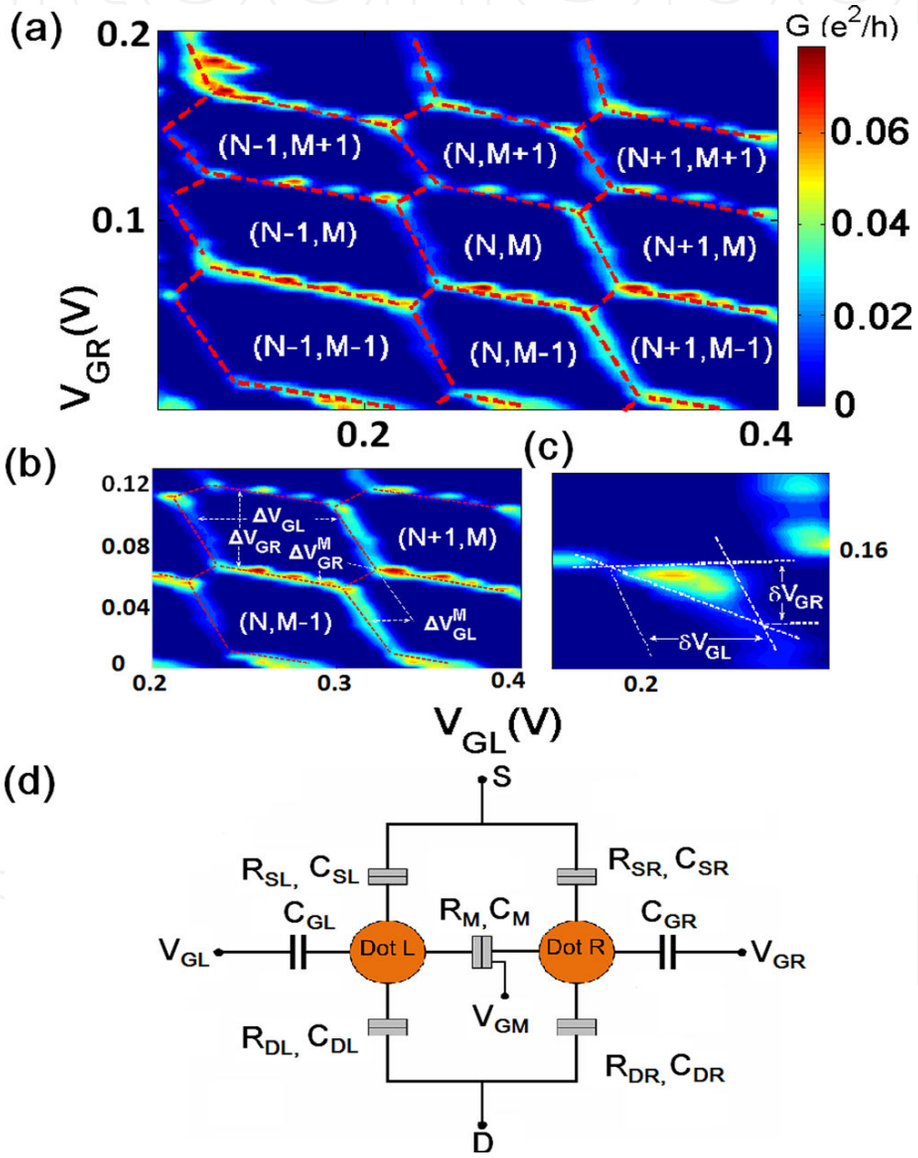

Figure 10. Color online) (a), (b), and (c) PDQD differential conductance as a function of plunger gate voltage V_{GL} and V_{GR}. The red dash lines are guides to the eyes showing the honeycomb pattern. (N,M) represents the carriers in the left and right dot, respectively. (b) Zoom-in of the area (N,M) of the honeycomb pattern. (c) Zoom-in of a vertex pair with white dash lines. (d) Capacitance model for the analysis of the double dot system. Graphene nanoconstrictions behave as tunneling barriers, which are presented, for example, as RSL, CSL (a capacitance and a resistance coupled in parallel). Gate GL and GR are capacitively coupled to the dots; C_{GL} and C_{GR} represent the capacitance.

Fig. 10(a) shows color scale plot of the measured differential conductance of the double dot as a function of V_{GL} and V_{GR} detected in standard ac lock-in technique with anexcitation ac voltage 20μV at frequency of 11.3 Hz. A dc bias of 0.3 mV is applied, the back gate voltage V_{bg} is fixed at 5 V and the middle plunger gate V_{GM} is -0.45 V. The hexagon pattern characteristic for double dot coupled in parallel is clearly visible. Figure 2(b) Zoom-in of the area (N, M) of the honeycomb pattern, Figure 2(c) Zoom-in of a vertex pair with white dashed lines. From the model of purely capacitively coupled dots as illuminated by Figure 2(d), the energy scales of the system can be extracted (van der Wiel et al., 2003; Molitor et al., 2010; Moriyama et al., 2009). The capacitance of the dot to the side gate can be determined from measuring the size of the honeycomb as shown in Fig. 10(a) and 10(b), ΔV_{GL} =0.087V, ΔV_{GR}=0.053V ,ΔV_{GL}^{m} =0.0261V ΔV_{GR}^{m}=0.0133V, therefore, C_{GL} =$e/\Delta V_{GL}$ =1.84aF,C_{GR}=$e/\Delta V_{GR}$=3.0aF. With a large DC bias of 0.3 mV, we can get δV_{GL} =0.013Vand δV_{GR}=0.01V as shown in Figure 2(c). The lever arm between the left (right) gate $V_{GL}$and the left (right) dot can be calculated as α_{GL} =$V_{bias}/\delta V_{GL}$ =0.023(α_{GR}=$V_{bias}/\delta V_{GR}$=0.03). The total capacitances of the dots can then be calculated as C_L =C_{GL} /α_L =79.8aFandC_R=C_{GR}/α_R=100.4aF, the corresponding charging energyE_{CL} =α_{GL} .ΔV_{GL} =2.0meVandE_{CR}=α_{GR}.ΔV_{GR}=1.6meV, the coupling energy between the two dotsE_{CM}=α_{GL} .ΔV_{GL}^{m} =0.3meV. It is also noted that the lever arms between the left gate and the right dot and vice versa can be determined from the slope of the co-tunneling lines delimiting the hexagons. These crossing couplings only modify the results slightly and are neglected usually (Molitor et al., 2010; Moriyama et al., 2009; Liu et al., 2010). Here, by calculating dots area and carrier density (related to V_{BG}), or from the Coulomb charging period, we estimate each dot contains more than 20 electrons when V_{BG}=5V.

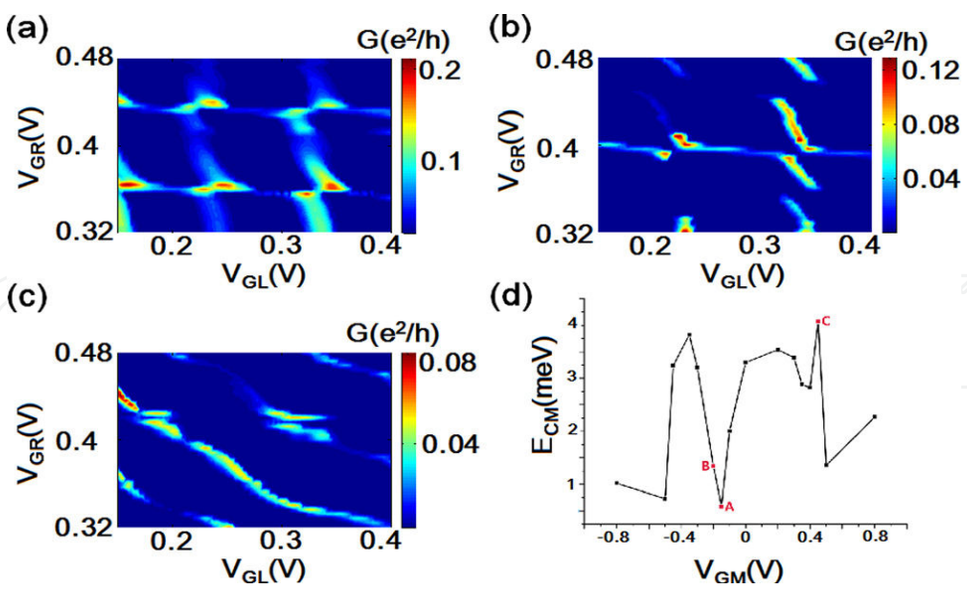

Figure 11. Color online) Interdot coupling vs middle gate voltage V_{GM}. Conductance as a function of gate voltage V_{GL} and V_{GR} at V_{BG}=3 V, V_{bias}=- 1 mV, the scan regions of GL and GR are the same. (a), (b), and (c) represent three different coupling regimes of the two dots. (a) weak coupling regime, V_{GM}= -0.15 V, (b) medium coupling regime, V_{GM}= -0.2 V (c) strong coupling regime, V_{GM}= 0.45 V. (d) shows coupling energy E_{CM} (V) as a non-monotonic function of the middle gate voltage V_{GM}. A, B, C point here represent the corresponding coupling energy in (a), (b), and (c).

By applying voltage to the middle plunger gate GM, the interdot coupling can be tuned efficiently. Fig.11(a), 11(b),and 11(c) show the charge stability diagrams of the PDQD in three different coupling regimes. [(a) weak, (b) medium, and (c) strong]. In these measurements, back gate voltage V_{BG} =3V, Source-Drain DC bias V_{bias} is set to-1.0mV, the scan regions of GL and GR are the same. Only the voltage applied to the gate GM is adjusted as (a) V_{GM}= -0.15 V, (b) V_{GM}=0.2 V, and (c) V_{GM}=0.45 V. By using the same model as in Figure 2, we can calculate the corresponding coupling energy between the dots: (a) E_{CM}=0.58 meV, (b) E_{CM}=1.34 meV, and (c) E_{CM}=4.07 meV. The honeycomb diagrams of the parallel and serial DQD look similar except for the weak coupling regime, as shown in Figure3(a). In this case, the lines delimiting the hexagons are more visible in comparison with serial DQD, because the leads have two parallel accesses to the dots in parallel DQD, which also enables correlated tunneling of two valence electrons simultaneously (Holleitner et al., 2002). Fig. 11(d) indicates the coupling energy changes with the gate voltage VGM. As in the previous reports of graphene DQD in series (Molitor et al., 2010; Liu et al., 2010), the inter-dot coupling is non-monotonically depended on the applied gate voltage. Although the detailed reasons for this non-monotony are undetermined, we assumed that one key factor will be the disorders in graphene introduced by either fabrication steps or substrate (Todd et al., 2009). Many more efforts are still needed to address this issue for the realization of practical graphene based nanodevices.

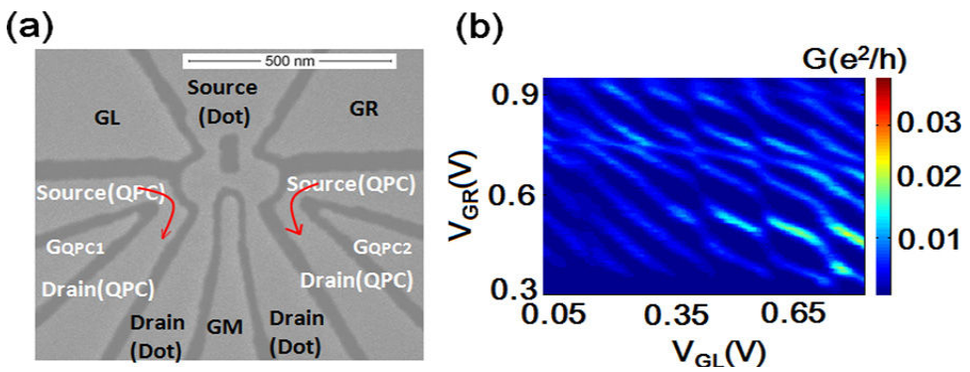

Figure 12. Color online) (a) SEM image of single layer graphene PDQD integrated with two QPCs. The bar has a length of 500 nm. (b) Characteristic honeycomb structure of the conductance through the PDQD as a function of two in-plane plunger gates voltage V_{GL} and V_{GR}, revealed by direct transport measurement of the PDQD at 4.2 K.

We have designed and fabricated an alternative structure of a PDQD integrated with two quantum point contact sensors (QPCs) in single layer graphene, as shown in Figure 4(a). The integrated QPCs can be used as a non-invasive charge detector which may have various applications (van der Wiel et al., 2003; Hanson et al., 2007; Guo et al., 2001; Zhang et al., 2007). As primary tests of the present structure, we can get similar charge stability diagram of the PDQD as in Fig.12 (b) by the direct quantum transport tests at 4.2 K. Although the non-invasive measurements by QPC are still under processing, no remarkable difference is founded between PDQD in bilayer and monolayer graphenes from direct transport measurement. Making tunable coupling double dot is the first step towards the quantum dot based quantum computation bits, the architectonics with integrated charge detector around double quantum dot demonstrated here offers the chance to achieve the charge or spin reading out,

which is essential for the quantum computation device. Therefore, a lot of extended and follow-up works can be done on this basis in the future. Both bilayer and single layer graphenes can be exploited in this application.

In summary, we have discussed low temperature quantum transport measurement of gate-controlled parallel coupled double quantum dot on both bilayer and single layer graphenes. The inter-dot coupling strength can be largely tuned by graphene in-plane gates. With the quantum transport honeycomb charge stability diagrams, a common model of purely capacitively coupled double dot is used to extract all the relevant energy scales and parameters of grapheme PDQD. Although many more effects are still needed to further upgrade and exploit the present designed grapheme quantum dot system, the results have intensively demonstrated the promise of the realization of graphene nanodevice and desirable study of rich PDQD physical phenomena in graphene.

5. Conclusion

To conclude, we have discussed the design and fabrication of etched gate tunable single and double quantum dots in single-layer and bilayer graphene and present several important quantum transport measurements in these systems. A quantum dot with an integrated charge sensor is becoming a common architecture for a spin or charge based solid state qubit. To implement such a structure in graphene, we have fabricated a twin-dot structure in which the larger QD serves as a single electron transistor (SET) to read out the charge state of the nearby gate controlled small QD. A high SET sensitivity of $10^{-3}e/\sqrt{Hz}$ allowed us to probe Coulomb charging as well as excited state spectra of the QD, even in the regime where the current through the QD is too small to be measured by conventional transport means. We also have measured quantum transport properties of gates controlled parallel-coupled double quantum dots (PDQD) and series-coupled double quantum dots (SDQD) device on both single layer and bilayer graphene with multiple electrostatic gates that are used to enhance control to investigate it. At low temperatures, the transport measurements reveal honeycomb charge stability diagrams which can be tuned from weak to strong inter-dot tunnel coupling regimes. We precisely extract a large inter-dot tunnel coupling strength for this system allowing for the observation of tunnel-coupled molecular states extending over the whole series-coupled double dot. The inter-dot coupling strength also can be effectively tuned from weak to strong by in-plane plunger gates for parallel-coupled double quantum dots. All the relevant energy scales

and parameters can be extracted from the honeycomb charge stability diagrams. The present method of designing and fabricating graphene DQD is demonstrated to be general and reliable and will enhance the realization of graphene nanodevice and desirable study of rich DQD physical phenomena in graphene, and highly controllable system serves as an essential building block for quantum devices in a nuclear-spin-free world.

Acknowledgments

This work was supported by the National Basic Research Program of China (Grants No. 2011CBA00200 and 2011CB921200), and the National Natural Science Foundation of China (Grants No. 10934006, 11074243, 11174267, 91121014, and 60921091)

Author details

Hai-Ou Li, Tao Tu, Gang Cao, Lin-Jun Wang, Guang-Can Guo and Guo-Ping Guo

Key Laboratory of Quantum Information, University of Science and Technology of China, Chinese Academy of Sciences, Hefei, P.R. China

References

[1] Berman D, Zhitenev N. B, Ashoori R. C, and Shayegan M, Phys. Rev. Lett. 82, 161 (1999).

[2] Bylander J, Duty T, and Delsing P, Nature London 434, 361 (2005).

[3] Chen J. C, Chang A. M, and Melloch M. R., Phys. Rev. Lett. 92, 176801 (2004).

[4] Dias da Silva L. G. G. V, Ingersent K, Sandler N, and Ulloa S. E, Phy. Rev. B 78, 153304 (2008).

[5] Duty T, Gunnarsson D, Bladh K, and Delsing P, Phys. Rev. B 69, 40503(R) (2004).

[6] Elzerman J. M, Hanson R, L. van Beveren H. W, L. Vandersypen M. K, and Kouwenhoven L. P, Appl. Phys. Lett. 84, 4617 (2004b).

[7] Elzerman J. M, Hanson R, van Beveren L. H. Witkamp W, B, Vandersypen L. M. K, and L. P. Kouwenhoven, Nature London 430, 431 (2004a).

[8] Fischer J, Trauzettel B, and Loss D, Phys. Rev. B 80, 155401 (2009).

[9] Fischer J. and Loss D, Science 324, 1277 (2009).

[10] Foletti S, Bluhm H, Mahalu D, Umansky V, and Yacoby A, Nat. Phys. 5, 903 (2009).

[11] Gallagher P., Todd K., and Goldhaber-Gordon D., Phys. Rev. B 81, 115409 (2010).

[12] Geim A. K and Novoselov K. S, Nature Mater. 6, 183 (2007).

[13] Geim A. K., Science 324, 1530 (2009).

[14] Golovach V. N, and Loss D, Phys. Rev. B 69, 245327 (2004).

[15] Gotz G, Steele G. A, Vos W. J, and Kouwenhoven L. P, Nano Lett. 8, 4039 (2008).

[16] Graber M. R, Coish W. A, Hoffmann C, Weiss M, Furer J, Oberholzer S, Loss D, and Scho°nenberger C, Phys. Rev. B 74, 075427 (2007).

[17] Guo G. P, Li C. F, and Guo G. C, Phys. Lett. A 286, 401 (2001).

[18] Guo G. P, Lin Z. R, Tu T, Cao G, Li X. P, and Guo G. C, New J. Phys.11, 123005 (2009).

[19] Güttinger J, Seif J, Stampfer C, Capelli A, Ensslin K, and Ihn T, Phys. Rev. B 83, 165445 (2011).

[20] Güttinger J, Stampfer C, Hellmüller S, Molitor F, Ihn T, and Ensslin K, Appl. Phys. Lett. 93, 212102 (2008).

[21] Hanson R, Kouwenhoven L. P, Petta J. R, Tarucha S, and Vandersypen L. M. K, Rev. Mod. Phys. 79, 1217 (2007).

[22] Hanson R, Witkamp B, Vandersypen L. M. K, van Beveren L. H. W, Elzerman J. M, and Kouwenhoven L. P, Phys. Rev. Lett. 91, 196802 (2003).

[23] Hanson R. and Awschalom D, Nature 453, 1043 (2008)

[24] Hatano T, Stopa M, and Tarucha S, Science 309, 268 (2005).

[25] Holleitner A. W, Blick R. H, Hu° ttel A. K, Eberl K, and Kotthaus J. P, Science 297, 70 (2002).

[26] Holleitner A. W, Decker C. R, Qin H, Eberl K, and Blick R. H, Phys. Rev. Lett. 87, 256802 (2001).

[27] Huard B, Sulpizio J. Stander A, Todd N. K, Yang B, and Goldhaber Gordon D, Phys. Rev. Lett. 98, 236803 (2007).

[28] Ihn T., Guttinger J, Molitor F, Schnez S. Schurtenberger E, Jacobsen A, Hellmu°ller S, Frey T, Droscher S, Stampfer C. et al., Mater. Today 13, 44 (2010).

[29] Knobel G. and Cleland A. N., Nature London 424, 291 (2003).

[30] Kouwenhoven L. P, Marcus C, McEuen P. L, Tarucha S, Westervelt R. M, and N. S. Wingreen, in Mesoscopic Electron Transport, Series E:Applied Sciences Vol. 345, edited by Sohn L. L, Kouwenhoven L. P, and Schon G, Dordrecht Kluwer, 1997, pp. 105–214.

[31] L. Ponomarenko, F. Schedin, Katsnelson M, Yang R, Hill E, Novoselov K, and Geim A, Science 320, 356 (2008).

[32] Ladro´n de Guevara M. L, Claro F, and Orellanal P. A, Phys. Rev. B 67, 195335 (2003).

[33] LaHaye D, Buu O, Camarota B, and Schwab K. C, Science 304, 74 (2004).

[34] Lehnert K. W, Bladh K, Spietz L. F, Gunnarsson D, Schuster D. I, Delsing P, and Schoelkopf R. J, Phys. Rev. Lett. 90, 027002 (2003).

[35] Liu X. L, Hug D, and L. Vandersypen M. K. Nano Lett. 10, 1623 (2010).

[36] Livermore C, Crouch C. H, Westervelt R. M, Campman K. L, and A. Gossard C, Science 274, 1332 (1996).

[37] Lo´pez R, Aguado R, and Platero G, Phys. Rev. Lett. 89, 136802 (2002).

[38] Lu W, Ji Z. Q, Pfeiffer L, K. W. West, and A. J. Rimberg, Nature London 423, 422 (2003).

[39] Mason N, Biercuk M. J, and Marcus C. M, Science 303, 655 (2004).

[40] Molitor F, Droscher S, Guttinger J, Jacobson A, Stampfer C, Ihn T, and Ensslin K, Appl. Phys. Lett. 94, 222107 (2009).

[41] Molitor F, Knowles H, Droscher S, Gasser U, Choi T, Roulleau P, Guttinger J, Jacobsen A, Stampfer C, Ensslin K. et al., Europhys. Lett. 89, 67005 (2010).

[42] Moriyama S, Tsuya D, Watanabe E, Uji S, Shimizu M, T. Mori, T. Yamaguchi, and Ishibashi K, Nano Lett. 9, 2891 (2009).

[43] Novoselov K. S, Geim A. K, Morozov S. V, Jiang D, Zhang Y, Dubonos S. V, Grigorieva I. V, and Firsov A. A, Science 306, 666 (2004).

[44] Orellana P. A, Ladron de Guevara M. L, and Claro F, Phys. Rev. B 70, 233315 (2004).

[45] Petta J. R, Johnson A. C, Taylor J. M, Laird E. A, Yacoby A, Lukin M. D , Marcus C. M, Hanson M. P, and Gossard A. C, Science 309, 2180 (2005).

[46] Ponomarenko L, Schedin F, Katsnelson M, Yang R. Hill E, Novoselov K, and Geim A. K, Science 320, 356 (2008).

[47] Schnez S, Molitor F, Stampfer C, Guttinger J, Shorubalko I, Ihn T, and Ensslin K, Appl. Phys. Lett. 94, 012107 (2009).

[48] Stampfer C, Guttinger J, F. Molitor, D. Graf, T. Ihn, and K. Ensslin, Appl. Phys. Lett. 92, 012102 (2008a).

[49] Stampfer C, Schurtenberger E, Molitor F, Guettinger J, Ihn T, and Ensslin K, Nano Lett. 8, 2378 (2008b).

[50] Stampfer C., Güttinger J., Hellmüller S., Molitor F., Ensslin K., and Ihn T., Phys. Rev. Lett. 102, 056403 (2009).

[51] Todd K, Chou H. Amasha T, S, and Goldhaber-Gordon D, Nano Lett. 9, 416 (2009).

[52] Trauzettel B, Bulaev D. V, Loss D, and Burkard G, Nat. Phys. 3, 192 (2007).

[53] van der Wiel W. de Francheschi G, S, Elzermann J. M, Fujisawa T, Tarucha S, and Kouwenhoven L P, Rev. Mod. Phys. 75, 1 (2003).

[54] Vijay R, M. H. Devoret, and I. Siddiqi, Rev. Sci. Instrum. 80, 111101 (2009).

[55] Vink I. T, Nooitgedagt T, Schouten R. N, and Vandersypen L. M. K, Appl. Phys. Lett. 91, 123512 (2007).

[56] Volk C, Fringes S, Terres B, Dauber J, Engels S, Trellenkamp S, and Stampfer C,.Nano Lett. 11, 3581 (2011).

[57] Wang L. J, Cao G, Li H. O, Tu T, Zhou C, Hao X. J, Guo G. C, and Guo G. P, Chinese .Physics. Letters. 28, 067301 (2011b).

[58] Wang L. J, Cao G, Tu T, Li H. O, Zhou C, Hao X. J, Su Z, Guo G. C, Jiang H. W, and Guo G. P, Appl. Phys. Lett. 97, 262113 (2010).

[59] Wang L. J, Guo G. P, Wei D, Cao G, Tu T, Xiao M, Guo G. C, and Chang A.M, Appl. Phys. Lett. 99, 112117 (2011a).

[60] Wang L. J, Li H. O, Tu T, Cao G, Zhou C, Hao X. J, Su Z, Xiao M, Guo G. C, Chang A.M, and Guo G. P, Appl. Phys. Lett. 100, 022106(2012).

[61] Yang S, Wang X, and Das Sarma S, Phys. Rev. B 83, 161301(R) (2011).

[62] Zhang H, Guo G. P, Tu T, and Guo G. C, Phys. Rev. A 76, 012335 (2007).

[63] Ziegler R, Bruder C, and Schoeller H, Phys. Rev. B 62, 1961 (2000).